

A Solution to the Problem of Phaseless Mapping for a High-Orbit Space-Ground Radio Interferometer

A. T. Bajkova

Main (Pulkovo) Astronomical Observatory, St.Petersburg, Russia

Received January 20, 2005; in final form, May 18, 2005

Abstract — We consider the problem of mapping with ultra-high angular resolution using a space–ground radio interferometer with a space antenna in a high orbit, whose apogee height exceeds the radius of the Earth by a factor of ten. In this case, a multielement interferometer essentially degenerates into a two-element interferometer. The degeneracy of the close-phase relations prevents the use of standard methods for hybrid mapping and self-calibration for the correct reconstruction of images. We propose a new phaseless mapping method based on methods for the reconstruction of images in the complete absence of phase information, using only the amplitudes of the spatial-coherence function of the source. In connection with this problem, we propose a new method for the reliable solution of the phase problem, based on optimizing information-carrying nonlinear functionals, in particular, the Shannon entropy. Results of simulations of mapping radio sources with various structures with ultra-high angular resolution in the framework of the RADIOASTRON mission are presented. ©2005 Pleiades Publishing, Inc.

1. INTRODUCTION

The problem of phaseless mapping in Very Long Baseline Interferometry (VLBI) is considered in detail in [1], together with the uniqueness of the solutions and methods for solving for the phases. The current study is a logical continuation of this work, since it is concerned with the phaseless mapping of radio sources with ultra-high angular resolution using a ground–space interferometer with a high-apogee orbiting antenna, and the development of more trustworthy methods for the reconstruction of images based only on the amplitudes of their Fourier spectra (the spatial-coherence function).

The problem of phaseless mapping in VLBI arises when the measured phases are subject to large errors introduced by the medium through which the radio wave propagates, and it is not possible to use the closure phases and adaptive-calibration methods (hybrid mapping and self-calibration [2]) traditionally applied in VLBI to correctly reconstruct images.

This is the case for a two-element interferometer [1], and also for a ground–space radio interferometer with an antenna in a high orbit whose apogee exceeds the Earth’s radius by an order of magnitude or more. In the latter case, the multi-element interferometer essentially degenerates into two elements, independent of the number of ground stations, leading to degeneracy in the phases summed around triangles. As a result, mapping using the standard methods becomes mean-

ingless.

This problem is relevant for the future Russian space mission RADIOASTRON [3] (planned to have an antenna in a high-apogee orbit reaching heights of 350 000 km), intended to map extragalactic radio sources with ultra-high angular resolution reaching hundredths of a milliarcsecond (mas), with the goal of revealing the workings of the central engines of distant quasars and galaxies.

As we indicated above, an effective strategy for phaseless VLBI mapping was presented in [1]. This method is based on (1) making a preliminary reconstruction of the amplitude of the visibility function (spectrum) over the entire *UV* plane by reconstructing an intermediate image with zero spectral phase using the data measured on a limited set of points, and (2) reconstructing the desired image based on the amplitude of the source spectrum obtained in the first stage using methods designed to solve the phase problem.

The goal of our current study is to develop a method for the realization of the second step of this algorithm that is more reliable than the method of Fienup that has been applied earlier.

The goal of this work is topical. In spite of the fundamental existence (apart from degenerate cases, defined on a set of measure zero) of solutions of the phase problem for multidimensional (≥ 2), spatially

restricted signals described by nonnegative real functions [4] that are unique with accuracy to within a class of equivalent functions (a linear shift or rotation of the image by 180°), no trustworthy, practical algorithm has been developed to obtain these solutions. For example, the algorithms of Fienup [5,6], which are the most efficient and most widely applied in practice, do not possess the property of compression [7], so that they cannot guarantee convergence to the correct solution in all cases. A successful application of Fienup algorithms in the case of comparatively simple source structures is demonstrated in [1].

Here, we attempt to fill this gap by proposing a more fundamental method for solving the phase problem, based on using the methods of nonlinear optimization to search for global extrema.

The following sections discuss VLBI mapping with an antenna in a high orbit, describe the proposed method for solving the phase problem, and present tests of the method and results of simulations of the RADIOASTRON mission, aimed at mapping radio sources with ultra-high angular resolution.

2. VLBI MAPPING WITH AN ANTENNA IN A HIGH ORBIT

Placing at least one VLBI station beyond the Earth, and thereby increasing the maximum baseline of the resulting interferometer, makes it possible to appreciably enhance the resolving power of the instrument.

It is planned in the near future to realize the space project RADIOASTRON [3] of the Russian Academy of Sciences (the Astro Space Center, Lebedev Physical Institute), which aims to construct a ground-space radio interferometer for the mapping of radio sources with ultra-high angular resolution, of the order of hundredths of a mas. Such resolutions are provided by observations at 1.35 cm on the maximum baseline of 350 000 km, which is achieved when the orbiting antenna is at apogee [8].

The desire to obtain ultra-high angular resolution by increasing the length of the baseline joining the ground stations and the one orbiting station leads to certain mathematical problems in the mapping, associated with the degeneracy of the multielement ground-space interferometer into a two-element interferometer in terms of the effective filling of the *UV* plane, independent of the number of ground stations [1]. One consequence of this is the degeneracy of the relations for the closure phases that are traditionally used in VLBI to correctly reconstruct the spectral phases via adaptive-calibration methods.

We can write the equations for the closure phases [2]:

$$\begin{aligned} \tilde{C}_{ijk} &= \tilde{\phi}_{ij} + \tilde{\phi}_{jk} - \tilde{\phi}_{ik} = \\ &= \phi_{ij} + \phi_{jk} - \phi_{ik} + \text{noise term} = C_{ijk} + \text{noise term}, \end{aligned} \quad (1)$$

where $\tilde{\phi}_{ij} = \phi_{ij} + \theta_i - \theta_j + \text{noise term}$, ϕ_{ij} is the spectral phase of the source on the baseline (ij) , θ_i and θ_j are the phases of the complex gains of antennas i and j , which include both instrumental and atmospheric components that cancel out when the phases are summed around a triangle, and "noise" term is the random, residual component of the phase noise, which is usually small. Here, a tilda denotes measured quantities.

The degeneracy of the closure-phase equations is a consequence of the geometrical degeneracy of the triangles, whose apices correspond to the ground antennas i and j and the space antenna k , which is very distant from the Earth. The right-hand side of relation (1) essentially vanishes, independent of the real spectral phase of the source: $\tilde{C}_{ijk} \approx \text{noise term} \approx 0$. It is obvious that, in this situation, applying the closure equations will always yield symmetrical structures, independent of the real source structure.

The problem of poor *UV*-plane coverage, which leads to large sidelobes in the synthesized antenna beam, can be partially solved by applying the technique of multifrequency synthesis [9,10]. However, this is not sufficient to correctly reconstruct the phases. Therefore, we propose to use phaseless mapping based on the presented methods to reconstruct the structure of the source. We can correctly reconstruct the spatial orientation of the source using a solution obtained via adaptive-calibration methods based on observations with the ground-based (low-frequency) part of the VLBI array.

3. METHOD FOR SOLVING THE PHASE PROBLEM

Let us formulate the problem of reconstructing two-dimensional images in discrete form. Let the discretization of the map be carried out in accordance with the theorem of Kotelnikov-Shannon, and the dimensions of the map be $N \times N$. The spectrum of the source is the N -point discrete Fourier transform of the two-dimensional distribution x_{ml} over the source radiation with a finite carrier:

$$\begin{aligned} X_{nk} &= \frac{1}{N} \sum_{m=0}^{N-1} \sum_{l=0}^{N-1} x_{ml} \exp\left(\frac{-i2\pi(nm + kl)}{N}\right) = \\ &= A_{nk} + iB_{nk} = M_{nk} \exp(i\Phi_{nk}), \end{aligned} \quad (2)$$

where A_{nk} is the real part, B_{nk} the imaginary part, M_{nk} the magnitude, and Φ_{nk} the phase of the spectrum X_{nk} , with

$$A_{nk} = M_{nk} \cos \Phi_{nk}, \quad B_{nk} = M_{nk} \sin \Phi_{nk}. \quad (3)$$

We formulate this problem as follows. We wish to use known values of the amplitude of a spectrum

(the spatial-coherence function in VLBI) M_{nk} on some set of points in the spatial-frequency domain (the *UV* plane) to reconstruct the image x_{ml} , which is equivalent to reconstructing the spectral phase Φ_{nk} , since the distribution x_{ml} is the inverse Fourier transform of the total spectrum X_{nk} (2), taking into account both the amplitudes and phases.

Let the measurements of the spatial-coherence function taking into account (2) and (3) satisfy the relations

$$\sum_m \sum_l x_{ml} a_{ml}^{nk} + \eta_{nk}^r = A_{nk} = M_{nk} \cos \Phi_{nk}, \quad (4)$$

$$\sum_m \sum_l x_{ml} b_{ml}^{nk} + \eta_{nk}^i = B_{nk} = M_{nk} \sin \Phi_{nk}, \quad (5)$$

separately for the real and imaginary parts of the spectrum, where $a_{ml}^{nk} = \cos(2\pi(mn + lk)/N)/N$, $b_{ml}^{nk} = \sin(2\pi(mn + lk)/N)/N$, η_{nk}^r and η_{nk}^i are the measurement errors for the real and imaginary parts of the spectrum, respectively, which obey a Gaussian distribution with zero mean and dispersion σ_{nk}^2 .

Let us represent the relations for the spectral phase as follows:

$$\cos \Phi_{nk} = 2 \cos^2(\Phi_{nk}/2) - 1, \quad (6)$$

$$\sin \Phi_{nk} = (\sin(\Phi_{nk}/2) + \cos(\Phi_{nk}/2))^2 - 1 \quad (7)$$

The reconstruction of the image can then be represented as the solution of the following optimization problem with the linear constraints (4), (5), into which we substitute the variables t_{nk} and s_{nk} in accordance with (6)–(9):

$$\min Q(x_{ml}, t_{nk}, s_{nk}) + \sum_n \sum_k \frac{(\eta_{nk}^r)^2 + (\eta_{nk}^i)^2}{2\sigma_{nk}^2}, \quad (8)$$

$$\sum_m \sum_l x_{ml} a_{ml}^{nk} - M_{nk} t_{nk} + \eta_{nk}^r = -M_{nk}, \quad (9)$$

$$\sum_m \sum_l x_{ml} b_{ml}^{nk} - M_{nk} s_{nk} + \eta_{nk}^i = -M_{nk}, \quad (10)$$

$$x_{ml}, t_{nk}, s_{nk} \geq 0, \quad (11)$$

Here, Q is a nonlinear functional determining the chosen criteria for the quality of the reconstruction. The second term in the optimization functional (10) is an estimate of the disagreement between the solution and the measurements according to an χ^2 criterion.

In addition, it is easy to show that the variables t_{nk} and s_{nk} satisfy the nonlinear constraint

$$\cos^2 \Phi_{nk} + \sin^2 \Phi_{nk} = (t_{nk} - 1)^2 + (s_{nk} - 1)^2 = 1, \quad (12)$$

which is key for the correct reconstruction of the spectral phase.

Including the nonlinear constraints (14) in the Lagrange functional in the standard way appreciably complicates the reconstruction algorithm. We therefore propose the following scheme for the solution of problems (10)–(14). The problem with the linear constraints (10)–(13) is first solved in the standard way via direct optimization using Lagrange multipliers [7]. In the course of the numerical iterative search for the extremum of the corresponding dual functional (for example, using a coordinate-descent method [11]), the nonlinear constraints (14) are placed on the variables t_{nk} and s_{nk} , similar to a projection onto a convex set [7]. In this case, t_{nk} and s_{nk} cannot vary independently of each other in their determination of the spectral phase. This combined algorithm incorporates the advantages of both methods for the optimization of nonlinear functionals with linear constraints, characterized by the presence of a global extremum, and iterative methods, which are distinguished by the simplicity of their allowance for various constraints on the solution directly in the computational algorithm.

When Q is a functional of the Shannon entropy [12], namely,

$$Q(x_{ml}, t_{nk}, s_{nk}) = \sum_m \sum_l x_{ml} \ln x_{ml} + \sum_n \sum_k (t_{nk} \ln t_{nk} + s_{nk} \ln s_{nk}) \quad (13)$$

we have the maximum-entropy method (MEM). The basis for the legitimacy of the functional (15), which is the total entropy of the image and the new variables t_{nk} and s_{nk} , can be obtained based on a ray model for the formation of the image [7], maximizing the joint probability for the formation of the image and the field of the statistically independent variables $\{t_{nk}, s_{nk}\}$.

An important constraint appearing in the system of equations (11) and specified by the necessary normalization of the image is the constraint on the total flux of the source M_o (the zeroth harmonic of the spectrum):

$$\sum_m \sum_l x_{ml} = M_o.$$

Another well-studied effective method is the minimum measure of Rényi [13]. In this case, the functional Q has the appearance

$$Q(x_{ml}, t_{nk}, s_{nk}) = \sum_m \sum_l x_{ml}^\alpha + \sum_n \sum_k (t_{nk}^\alpha + s_{nk}^\alpha),$$

where $\alpha \neq 1$.

In practice, in VLBI mapping, the Shannon entropy has become the most widely accepted among the various nonlinear functionals specifying various measures of the quality of reconstructed images. Accordingly, we consider here a developed phase-reconstruction method based on the MEM.

Applying the standard Lagrange-multiplier method to problems (10)–(13) and using (15) yields the following absolute optimization problem:

$$\begin{aligned} \min \quad L = & \sum_m \sum_l x_{ml} \ln x_{ml} + \sum_n \sum_k (t_{nk} \ln t_{nk}) \quad (14) \\ & + s_{nk} \ln s_{nk}) + \sum_n \sum_k \frac{(\eta_{nk}^r)^2 + (\eta_{nk}^i)^2}{2\sigma_{nk}^2} \\ & + \sum_n \sum_k \alpha_{nk} (\sum_m \sum_l x_{ml} a_{ml}^{nk} - M_{nk} t_{nk} \\ & + \eta_{nk}^r + M_{nk}) + \sum_n \sum_k \beta_{nk} (\sum_m \sum_l x_{ml} b_{ml}^{nk} \\ & - M_{nk} s_{nk} + \eta_{nk}^i + M_{nk}), \end{aligned}$$

where α_{nk}, β_{nk} are the Lagrange multipliers, or the dual variables.

The necessary condition for the existence of an extremum of the functional L is that the gradient $\frac{\partial L}{\partial y_{op}} = 0$, and that the Hess matrix composed of the elements $\frac{\partial^2 L}{\partial y_{op} \partial y_{qr}}$ be positive semidefinite at the point where this gradient is zero (here, the letter y denotes the generalized variables $x_{ml}, t_{nk}, s_{nk}, \eta_{nk}^r, \eta_{nk}^i$, and op, qr the two-dimensional indices for these variables).

A sufficient condition for the existence of a local extremum is that the Hess matrix be positive definite. If the Hess matrix is positive definite everywhere, the functional will be convex, and the local extremum will be a global extremum.

We can obtain a solution for the desired distribution (image) x_{ml} and the variables t_{nk}, s_{nk} determining the spectral phase from the necessary condition for the existence of an extremum of the functional L :

$$x_{ml} = \exp(\sum_n \sum_k \alpha_{nk} a_{ml}^{nk} + \beta_{nk} b_{ml}^{nk} - 1), \quad (15)$$

$$t_{nk} = \exp(\alpha_{nk} M_{nk} - 1), \quad s_{nk} = \exp(\beta_{nk} M_{nk} - 1), \quad (16)$$

$$\eta_{nk}^r = -\alpha_{nk} \sigma_{nk}^2 \quad \eta_{nk}^i = -\beta_{nk} \sigma_{nk}^2.$$

As we can see from (17) and (18), the solutions for the variables x_{ml}, t_{nk}, s_{nk} are always positive; i.e., the condition (13) is satisfied automatically, which is an internal property of the entropy functional. It is not difficult to show that the Hess matrix is diagonal and has positive elements, which means that it is positive definite everywhere, so that the Lagrange functional (16) is convex and the solution is global, i.e., unique.

However, the uniqueness of the solution in this case refers only to the uniqueness of the reconstruction of the shape of the source. Images obtained as a result of linear shifts or 180° rotations of the solution (17) also satisfy (10)–(14), as follows from the properties of the trigonometric functions determining the desired phase in terms of the variables t_{nk} and s_{nk} [see (8), (9)], and so are likewise solutions of the functional (16). All these solutions comprise a class of equivalent functions that differ by linear shifts or rotations by 180° . Thus, the proposed method for solving the phase problem yields a unique solution with accuracy to within a class of equivalent functions. We used the coordinate-descent method studied in detail in [11] for various functionals to numerically realize the absolute optimization (16).

In addition, note that the proposed mapping method based on the MEM possesses higher stabilizing properties with respect to the noise than, for example, the CLEAN algorithm that is traditionally used in adaptive-calibration methods in VLBI, or the method of Fienup used in [1]. The high stability of the proposed method is due to both the properties of the nonlinear entropy functional and the possibility of including the real signal-to-noise ratio in the χ^2 criterion [see (10)][14].

4. TESTING THE METHOD

We tested the proposed method using the eight model radio sources shown in Fig.1. The models and the radio sources themselves will be referred to in accordance with the notation in the figure, using the letters "a–h". These models reflect the various characters of possible brightness distributions — from a collection of unresolved point sources and various numbers of Gaussian components with various relative positions, to uniform distributions within specified boundaries and rings (see the following section for more detail on these source structures). Note that the lowest contour and the constant step between contours in all images is 1% of the peak of the map.

Figure 2 shows the images reconstructed in the case of zero spectral phase. As was noted in Section 2, this is characteristic of situations in which the phase triangles are completely degenerate. These images were produced using standard mapping methods. We can see that the source structures have taken on a symmetrical form. Mapping methods that enable reconstruction of the spectral phase are required if we wish to derive the intrinsic structure of the source. Images obtained

using our proposed method to reconstruct the phases are presented in Fig.3.

We took the full set of measurements of the amplitude of the spectrum as the input data. A comparison of the model (Fig.1) and reconstructed (Fig.3) maps demonstrates the fairly high internal accuracy of the method, which is from 1% to 4% for these examples. We can see from Fig.3 that some sources are reconstructed with accuracy to within a linear shift ("g" and "h") or within a rotation by 180° ("c" and "d").

To test the application of the proposed method to real VLBI data, we carried out phaseless mapping of the radio source 2200 +420 using data obtained during a global astrometric/geodetic observing program at 8.2 GHz (wavelength 3.5 cm) in 1996–1997. The *UV*-plane coverages corresponding to these data are presented in [1]. Figure 4 shows images reconstructed with angular resolutions of the order of 0.5–0.7 mas. These maps qualitatively and quantitatively agree with the results obtained in [1] using alternative mapping methods — both phaseless methods based on the algorithm of Fienup and standard methods based on self-calibration. Real geodetic VLBI data are not intended for astrophysical mapping, and therefore do not have the highest quality in terms of calibration and signal-to-noise ratio. Nevertheless, our analysis of maps made from such data shows that the proposed method is able to construct high-quality images with resolutions determined by the geometry of the interferometer.

5. SIMULATIONS OF THE RAOASTRON MISSION

We will now present the results of simulating mapping radio sources using a ground–space VLBI system with the following parameters.

The ground stations used (the choice is not of fundamental importance here) were the Svetloe, Zelenchuk, and Badary stations of the QUASAR network. The wavelength of the simulated observations was 1.35 cm. In the case of multifrequency synthesis, we used a frequency band with a width equal to 30% of the frequency corresponding to the chosen wavelength. The orbit of the RAOASTRON spacecraft [8] is inclined to the equatorial plane by 51.5° and has an angle from the Vernal Equinox to the line of nodes of -45° , an angle from the line of nodes to perigee of 30° , and perigee and apogee heights of 20 000 and 350 000 km, respectively. The period of the spacecraft in its orbit around the Earth is 9.5 days.

Figures 5a and 5b depict the coverage of the *UV* plane obtained for the cases of single-frequency and multifrequency syntheses over a time equal to one period of the spacecraft around the Earth. The spatial frequencies are plotted along the *U* and *V* axes in units of 10^8 wavelengths.

Note that, since the bandwidth for the multifre-

quency synthesis images was taken to be no more than 30% of the central frequency, the effect of the frequency dependence on the images can be neglected. According to the estimates of [15], the influence on the synthesized image due to this effect is no more than 1%, even when the source has a large spectral index. Correcting for the frequency can lower this influence to 0.1%. Our aim here is only to demonstrate the effect of the multifrequency synthesis regime on the coverage of the *UV* plane, compared to the case of single-frequency synthesis. If a wider band is used for the frequency synthesis, this requires application of frequency corrections, in accordance with the well known algorithms described in [15].

These parameters for the mapping system correspond to a maximum angular resolution of $\lambda/D = 0.007$ mas, where λ is the wavelength and D is the maximum baseline of the ground–space interferometer. The resolution in the east–west direction is roughly half that in the north–south direction. The following simulations will show that, thanks to the application of nonlinear methods, it is possible to reconstruction the images with a resolution higher than that indicated above.

As the model radio sources depicted in Fig.1, we used simplified Gaussian models derived from maps on mas scales constructed from VLBA [16] data at 8.2 GHz, but translated to the angular scales considered here (tens of microarcsecond).

Thus, the model-source structures presented in Fig.1 represent (a) a collection of point features corresponding to the three brightest components in the source 1223+395 [17], (b) a core and short curved jet adjacent to the core (a model for the quasar 0215+015), (c) an extended core and a comparatively bright one-sided, extended jet (a model for the quasar 1607+268), (d) a core and weak, one-sided, extended jet (a model for the quasar 1022+194), (e) a core and two-sided, multicomponent, bright jet (a model for the quasar 0238–084), (f) a collection of several bright and weak Gaussian components in a region about 50 microarcsecond in diameter (a model for the unidentified radio source 0259+121), (g) a uniform brightness distribution within specified boundaries, and (h) a thin ring. These two last source structures ("g" and "h") are the most exotic and demanding in terms of obtaining acceptable images by extrapolating the spectral data to the high-frequency domain, and are considered here in order to demonstrate the limits of the proposed reconstruction method.

Figures 6 and 7 present the images reconstructed based on the amplitude data for both the single-frequency and multifrequency syntheses. Note that we added to the data uniform noise in the range $\pm 10\%$ of each measurement of the visibility function, which yielded an input signal-to-noise ratio for the algorithm

of about ten, in agreement with the sensitivity parameters for the RADIOMRON mission presented in [18].

We give here a qualitative analysis of the reconstruction results. We will not take into consideration rotations of the images by 180° . We will refer to single-frequency and multifrequency syntheses as the first and second cases, respectively.

Source "a". The quality of the reconstruction was slightly worse in the first than in the second case. We can see several false point features (artefacts), but their brightnesses are appreciably lower than the brightnesses of the correctly reconstructed features ($<4\%$ of the peak value). More than the other distortions, the false features that are located along a line passing through the center of the source manifest the incomplete reconstruction of the spectral phase. In the second case, these artefacts are not present. In the first case, the shape of the source and the amplitude ratios of the features are somewhat distorted, while it was possible to reconstruct the correct amplitude ratios in the second case. The brightnesses of the small number of point artefacts in the second case is no more than 1–2%. The point features were reconstructed with finite resolution, but with a resolution that is higher than that of the array used. The resolution in the north–south direction is about twice that in the east–west direction. In both cases, the coordinates of the source components were accurately reconstructed. This simulation is useful because it clearly demonstrates the resolving capability of the reconstruction method.

Source "b". In both cases, it was possible to reconstruct the core well, but the adjacent jet much more poorly; in the second case, however, the jet is manifest more distinctly. In the first case, the features are elongated in the upward direction (in amplitude), making the weak, extended feature virtually invisible. This can be explained by the redistribution of the high-frequency components of the spectrum as a result of the extrapolation of the data belonging to a limited number of tracks in the *UV* plane [1]. The larger the region occupied by the data, the more exact the values of the extrapolated spectrum. The level of false extended features in the maps does not exceed 2%.

Source "c". As in the previous example, the Gaussian components are elongated in amplitude in the first case, likewise due to the redistribution of the spectrum at high spatial frequencies. The reconstruction of the shapes of the components and their brightness ratios is more accurate in the second case. The level of false features does not exceed 1%.

Source "d". A fundamental difference of this source structure from that considered in the previous example is that the brightness of the jet is appreciably lower than that of the core. In this case, the reconstruction of the image is more complex, since the spectral phases are expressed less strongly. This was visible in

the results of the simulations, which are presented in the table (as an example of the most typical type of radio source). Compared to the previous simulation, the incomplete reconstruction of the phases led to a growth in the brightnesses of the false components, which could be taken to be a counterjet. In the second case, however, the quality of the image is much better; the shapes and amplitude ratios of the components are reconstructed more accurately, and the level of artefacts is reduced by a factor of two.

Source "e". In the first case, the direction of the jet is reconstructed well, but individual components in the jet are expressed appreciably worse (due to the lower resolution in the east–west direction) than in the model, although they are nonetheless resolved. The maximum level of extended false features is about 10%. In the second case, both the shapes (although there is some elongation) and amplitude ratios of the components are reconstructed well. The artefacts occupy fewer regions, and their level does not exceed 5%.

Source "f". In these simulations, we have approximately the same relative qualities of the maps obtained for the single-frequency and multifrequency synthesis data as in the previous example. In the first case, there is some smearing near adjacent components due to the lower resolution in the east–west direction. All the components except for the weakest were reconstructed fairly well in the second case, although we can also see some elongation of their shapes. The weakest pointlike component was not able to be reconstructed in either case, reflecting the comparatively low dynamical range of the resulting maps.

Source "g". In both cases, we have a fairly good reconstruction of the boundary of the source, although there are three fairly bright artefacts (about 8% of the peak brightness) adjacent to the outer boundary in the first case. The resulting brightness distribution inside the boundary is not uniform. The brightness of artefacts is appreciably lower in the second case; they do not press up against the boundaries of the source and they have a pointlike character. The brightness distribution inside the source is substantially more uniform.

Source "h". The shape of the ring is reconstructed more distinctly and with a larger number of features in the second case. In both cases, there are pointlike artefacts adjacent to the ring, but the shape of the ring is clearly traced.

Thus, our analysis of the results of each simulation demonstrates that we were able to obtain an acceptable reconstruction, even in the case of poor *UV*-plane coverage (the single-frequency synthesis), at least for those sources with comparatively simple core + jet structures (such as sources "c", "d"). The multifrequency synthesis provided appreciably more accurate reconstructions than the single-frequency synthesis, with this difference being more pronounced as the source structure became

more complex (see the models for sources "e"–"h"). In all eight of the simulations, the multifrequency synthesis enabled more accurate reconstruction of the shapes and amplitude ratios of the components, provided higher resolution, and lowered the level of artefacts.

Analysis of the results (Figs.6 and 7) shows that the reconstructed maps have a resolution exceeding that of the instrument, especially in the case of multifrequency synthesis (the maps of sources "e" and "f"), although a ratio of 2:1 is preserved for the resolution in the north–south and east–west directions. The achievement of higher resolution is due to the fact that the image-reconstruction method is based on the substantially nonlinear maximum-entropy method, which has the property of super-resolution; i.e., the ability to trace the spectrum outside the aperture of the instrument. This frequency extrapolation is more accurate in the case of multifrequency synthesis, due to the more complete coverage of the *UV* plane.

If we convolve the solutions obtained (Figs.6 and 7) with a "clean" beam corresponding to half the width of the main lobe of the synthesized "dirty" beam for the system, in order to use the most reliably reconstructed part of the spectrum and to avoid the effect of overdetermination of the spectrum, on average, we obtain maps with angular resolution of the order of 0.01 mas.

Thus, when measuring the visibility function with a signal-to-noise ratio of about ten using a radio interferometer with the geometry specified for the RADIOASTRON mission, we can achieve a resolution of no worse than 0.010 mas at 1.35 cm. At lower signal-to-noise ratios, an appreciable role in the optimized functional (10) begins to be played by the regularizing term χ^2 , which can lead to some loss of resolution. Estimates show that this loss will constitute a factor of about 1.5 for a signal-to-noise ratio of about three.

It follows that, when used together with multifrequency synthesis, the proposed method for phaseless mapping can be successfully applied to obtain maps of good quality on angular scales of the order of tens of mas for data obtained on the RADIOASTRON ground–space interferometer, when standard methods of adaptive calibration can not be used due to the degeneracy of the closure-phase equations.

6. CONCLUSION

The task of phaseless VLBI mapping is especially topical now, in connection with future radio interferometers that may include a space antenna in a high orbit whose apogee exceeds the radius of the Earth by a factor of several dozen or more. In this case, the closure-phase relations become degenerate, making application of the standard methods of adaptive calibration incorrect. Our results on simulations for the RADIOASTRON ground–space radio interferometer, de-

signed for imaging with ultra-high angular resolution, demonstrate the ability to achieve acceptable image reconstructions when our proposed phaseless mapping methods are used together with multifrequency synthesis techniques.

ACKNOWLEDGMENTS

The author is grateful to N.S.Kardashev and A. V. Stepanov for support of this work. This work was partially supported by the Basic Research Program of the Presidium of the Russian Academy of Sciences "Non-stationary Phenomena in Astronomy".

REFERENCES

1. A. T. Baikova, Pis 'ma Astron.Zh. **30**, 253 (2004) [Astron. Lett. **30**, 218 (2004)].
2. T. J. Cornwell and E. B. Fomalont, in *Synthesis Imaging in Radio Astronomy II. A Collection of Lectures from the Sixth NRAO/NMIMT Synthesis Imaging Summer School*, Ed. by G. B. Taylor, C. L. Carilli, and R. A. Perley (Astron. Soc. Pac., San Francisco, 1999); Astron. Soc. Pac. Conf. Ser. **180**, 187 (1999).
3. N. S. Kardashev, Exp. Astron. **7**, 329 (1997).
4. Yu. M. Bruck and L. G. Sodin, Opt. Commun. **30**, 304 (1979).
5. J. R. Fienup, Opt. Lett. **3**, 27 (1978).
6. J. R. Fienup, Appl. Opt. **21**, 2758 (1982).
7. G. I. Vasilenko and A. M. Taratorin, *Image Restoration* (Radio i Syaz', Moscow, 1986) [in Russian].
8. *RADIOASTRON (Space VLBI Project)*, http://www.asc.rssi.ru/radioastron/description/orbit_eng.htm.
9. *RADIOASTRON (Space VLBI Project)*, http://www.asc.rssi.ru/radioastron/description/mfs_eng.htm.
10. A. T. Bajkova, Preprint No. 24, IPA AN SSSR (Inst. Appl. Astron., USSR Acad. Sci., Leningrad, 1990).
11. A. T. Bajkova, Preprint No. 58, IPA RAN (Inst. Appl. Astron., Russian Acad. Sci., St.-Petersburg, 1993).
12. B. R. Frieden, J. Opt. Soc. Am. **62**, 511 (1972).
13. B. R. Frieden and A. T. Bajkova, Appl. Opt. **34**, 4086 (1995).
14. T. J. Cornwell, R. Braun, and D. S. Briggs, in *Synthesis Imaging in Radio Astronomy II. A Collection of Lectures from the Sixth NRAO/NMIMT Synthesis Imaging Summer School*, Ed. by G. B. Taylor, C. L. Carilli, and R. A. Perley (Astron. Soc. Pac., San Francisco, 1999); Astron. Soc. Pac. Conf. Ser. **180**, 151 (1999).
15. R. J. Sault and J. E. Conway, in *Synthesis Imaging in Radio Astronomy II. A Collection of Lectures from the Sixth NRAO/NMIMT Synthesis Imaging Summer School*, Ed. by G. B. Taylor, C. L. Carilli, and R. A. Perley (Astron. Soc. Pac., San Francisco, 1999); Astron. Soc. Pac. Conf. Ser. **180**, 419 (1999).
16. C. Ma and M. Feissel, IERS Technical Note No. 23 (1997).
17. D. R. Henstock, I. W. Browne, P. N. Wilkinson, *et al.*, Astrophys. J., Suppl. Ser. **100**, 1 (1995).
18. *RADIOASTRON (Space VLBI Project)*, http://www.asc.rssi.ru/radioastron/description/observations_eng.htm.

Translated by D. Gabuzda

Characteristics of the measurements and reconstructed images

Map	Peak input noise relative to the measured amplitude of the visibility function	Signal-to-noise ratio in the input data	Peak relative brightness of the map	Entropy of the map	Peak false feature, %
Fig. 1d	–	–	1.00	-28.65	–
Fig. 6d	0.1	11.67	0.93	-31.74	6
Fig. 7d	0.1	10.04	1.06	-33.07	3

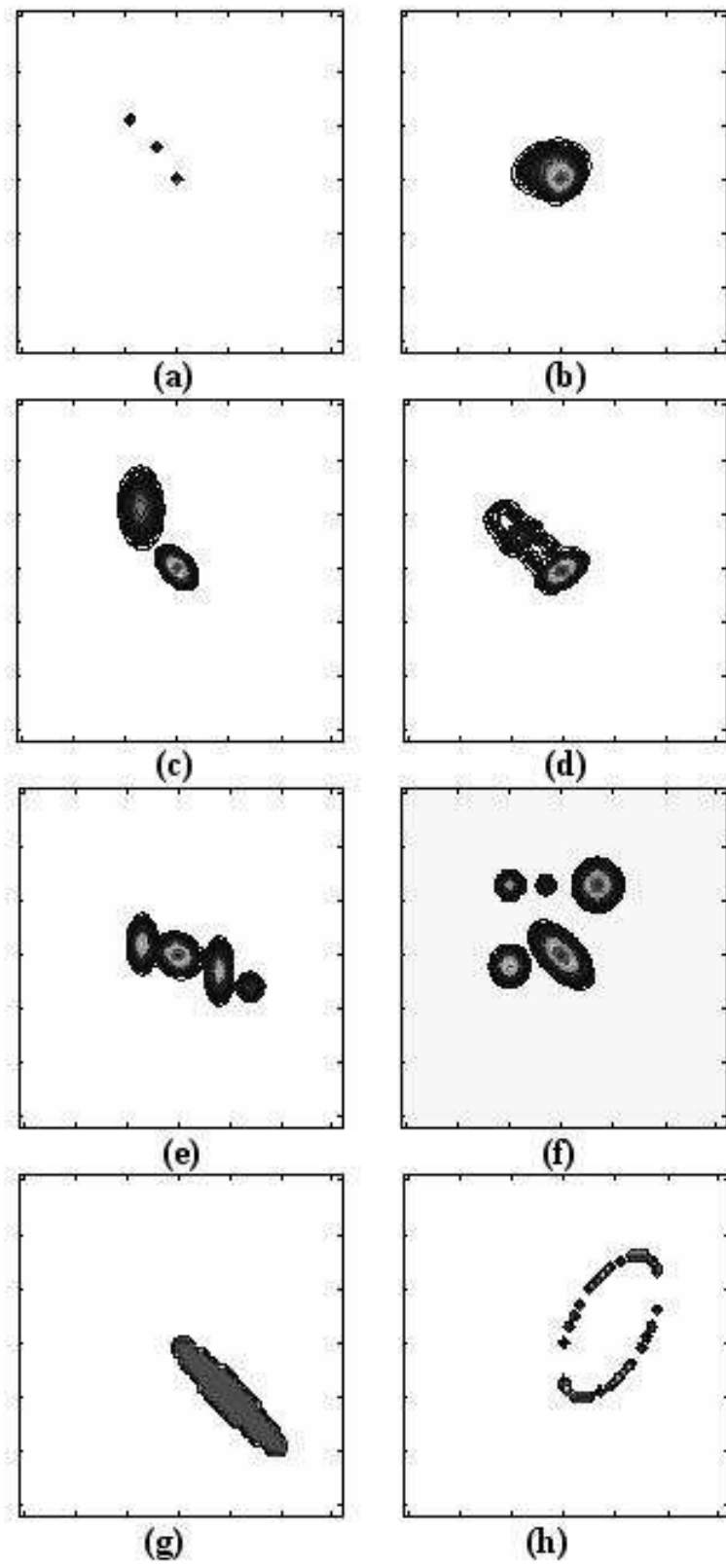


Fig.1. Specified images of model radio sources.

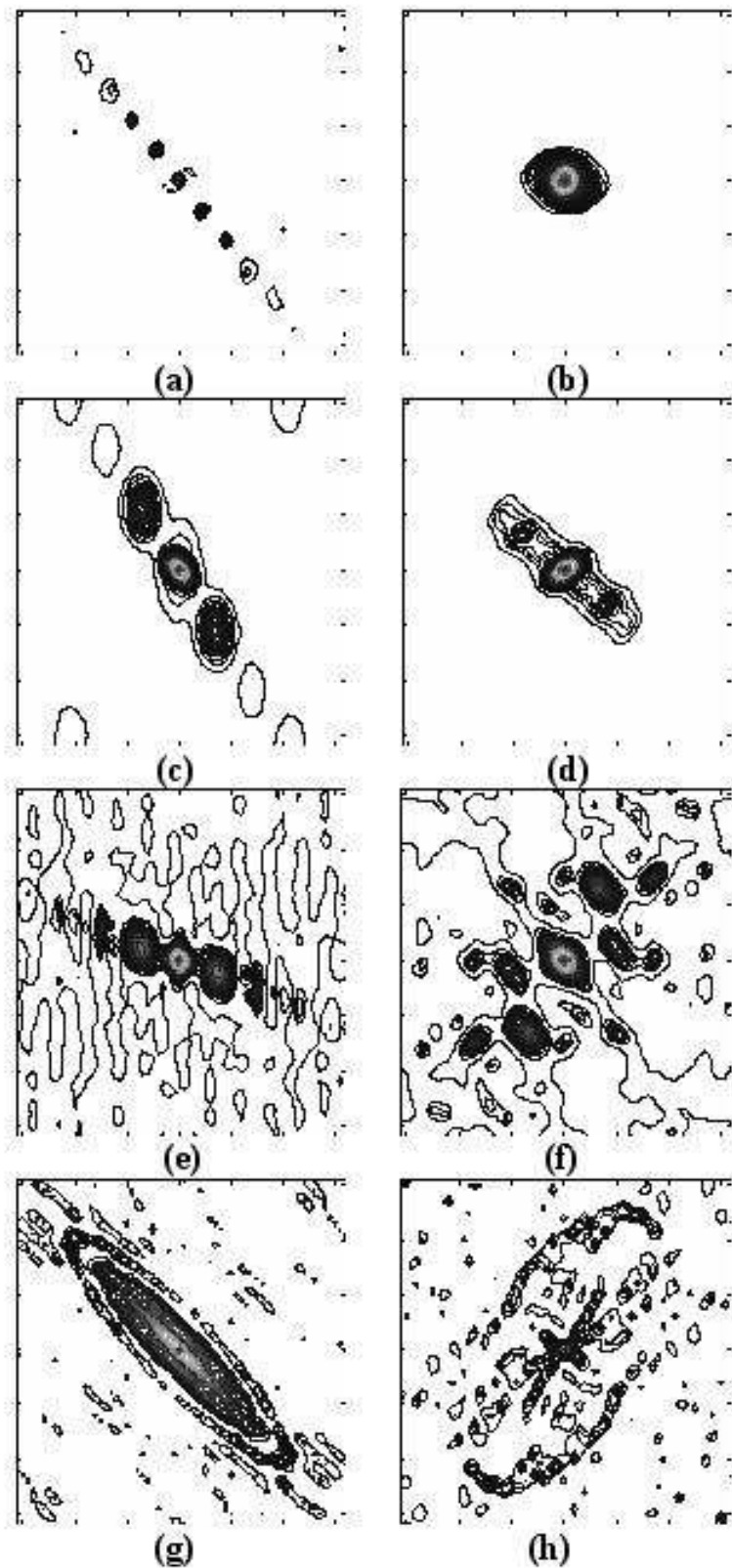


Fig.2. Images of model radio sources reconstructed using standard mapping methods in the case of degenerate phase triangles (zero spectral phase).

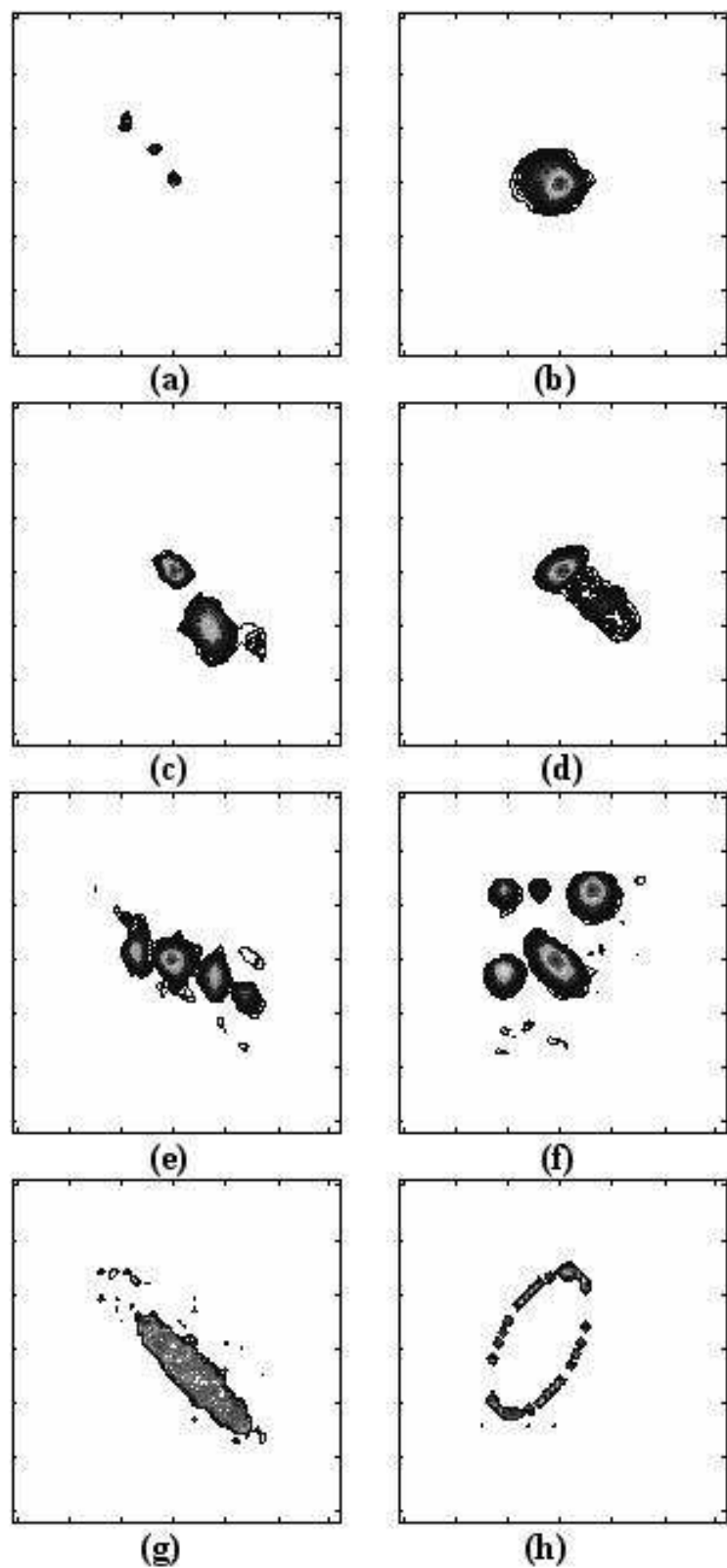
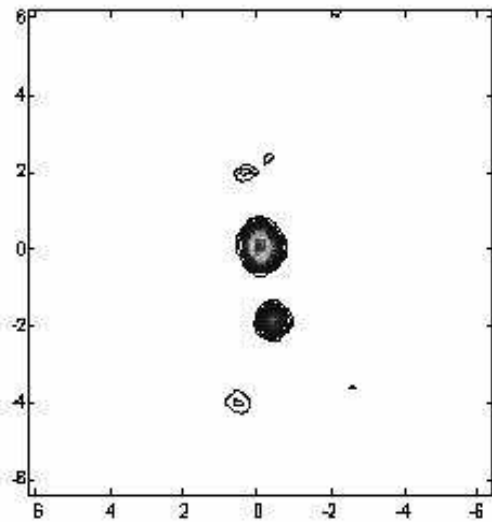
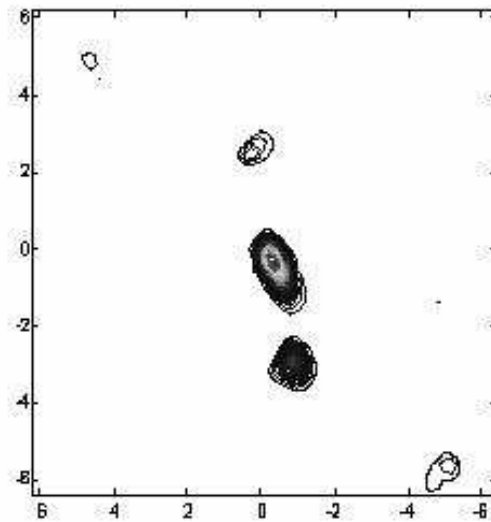


Fig.3. Images of the model radio sources constructed using the proposed phase-reconstruction method.

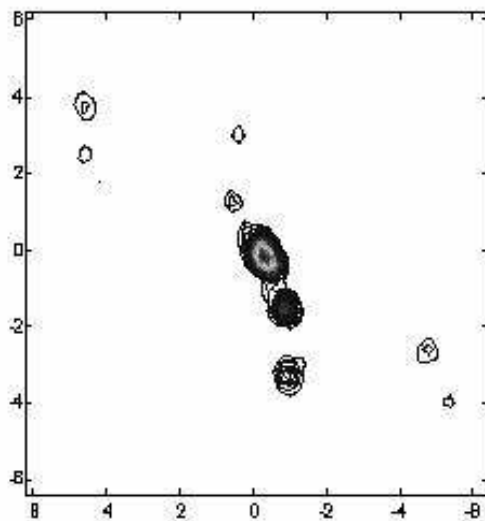
26 / 03 / 96



03 / 09 / 96



12 / 11 / 96



26 / 08 / 97

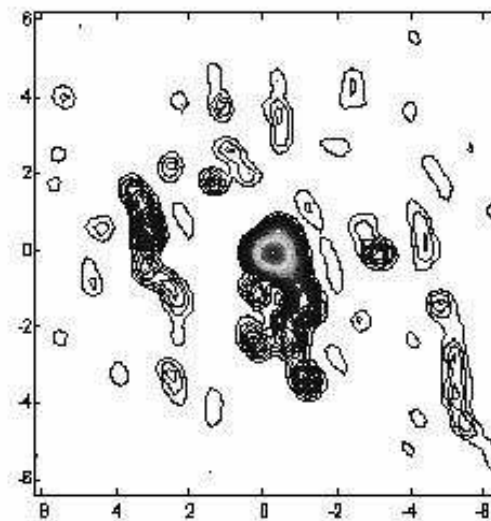


Fig.4. Results of mapping the radio source 2200+420 using data from a global VLBI array. The scales along the axes are in mas.

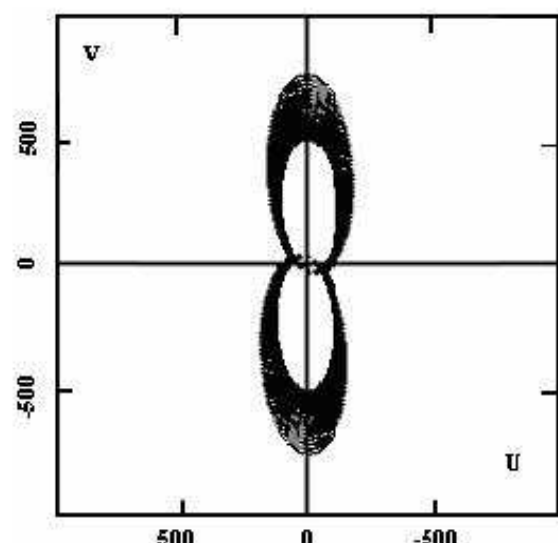
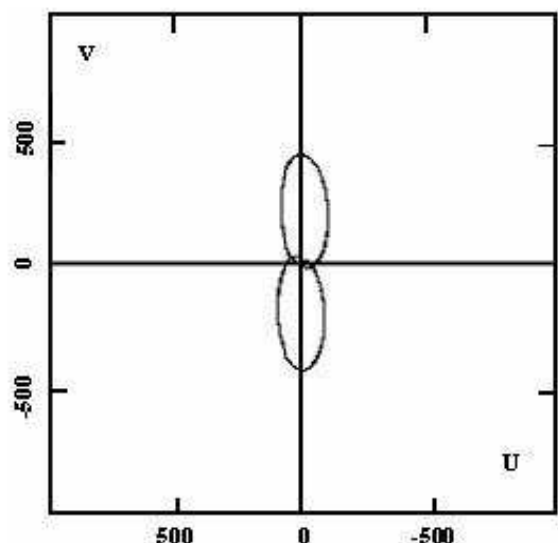
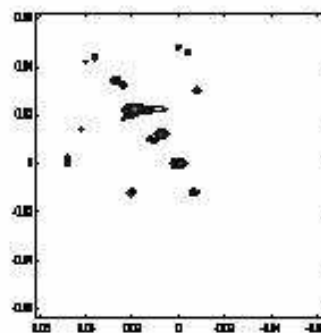
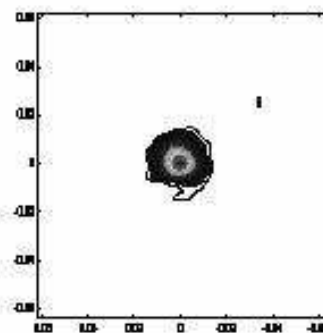


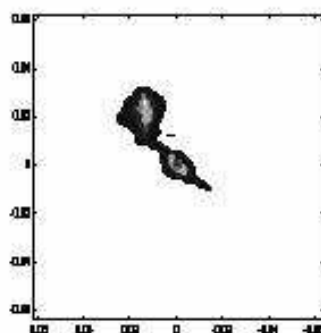
Fig.5. Simulations of a ground–space interferometer for (a) single-frequency synthesis and (b) multifrequency synthesis. The scales along the axes are in units of 10^8 wavelengths.



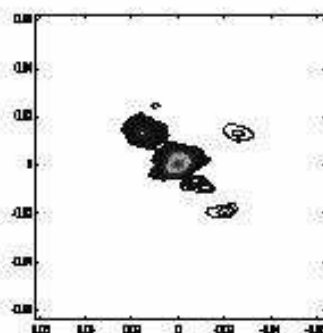
(a)



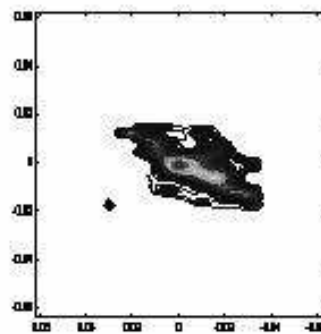
(b)



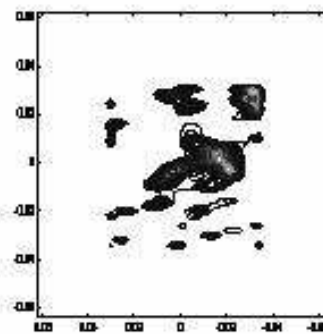
(c)



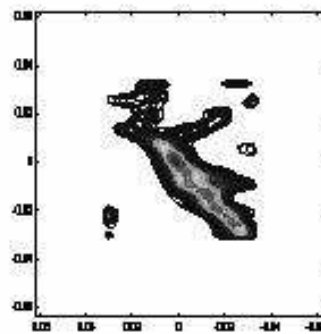
(d)



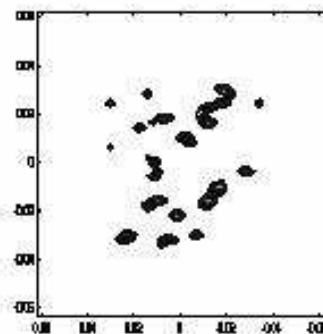
(e)



(f)

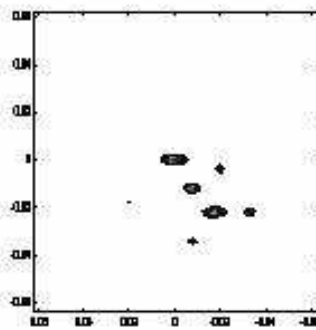


(g)

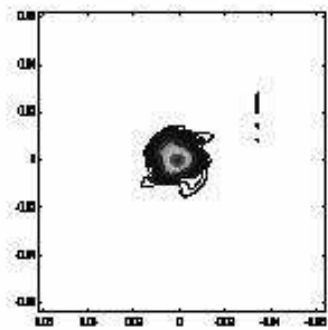


(h)

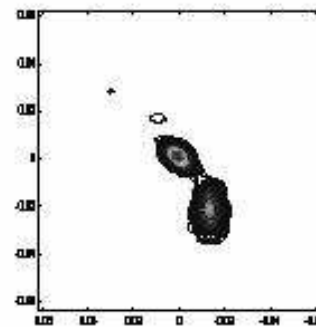
Fig.6. Images of model radio sources constructed from model single-frequency data for a ground-space interferometer with the parameters of RADIOASTRON. The scales along the axes are in mas.



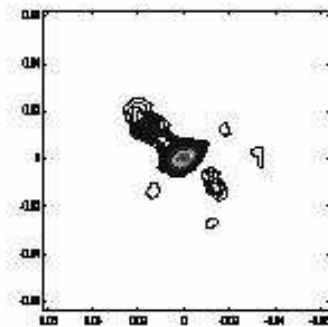
(a)



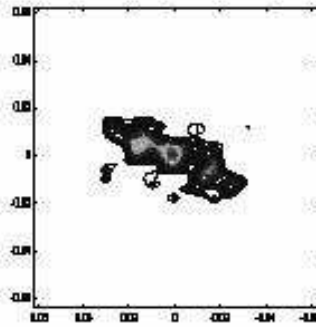
(b)



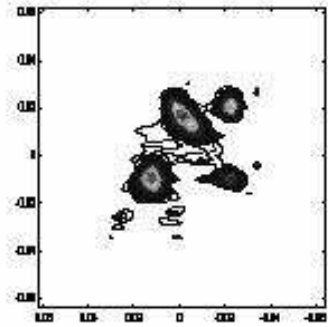
(c)



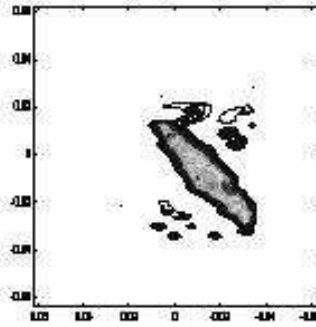
(d)



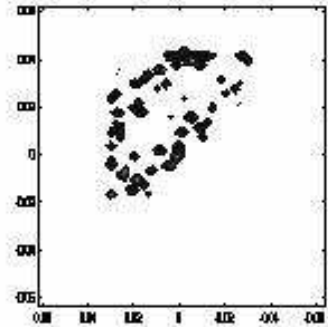
(e)



(f)



(g)



(h)

Fig.7. Same as Fig.6 but for multifrequency model data.